remote sensing

MDPI

Technical Note

Retrieval of Water Cloud Optical and Microphysical Properties from Combined Multiwavelength Lidar and Radar Data

Yinchao Zhang [1], Su Chen [1], Wangshu Tan [1,*], Siying Chen [1], He Chen [1], Pan Guo [1], Zhuoran Sun [1], Rui Hu [1], Qingyue Xu [1], Mengwei Zhang [1], Wei Hao [1] and Zhichao Bu [2]

[1] School of Optics and Photonics, Beijing Institute of Technology, Beijing 100081, China; ychang@bit.edu.cn (Y.Z.); su_chen@bit.edu.cn (S.C.); csy@bit.edu.cn (S.C.); shinianshao@bit.edu.cn (H.C.); guopan@bit.edu.cn (P.G.); szr@bit.edu.cn (Z.S.); 3220200423@bit.edu.cn (R.H.); 3120200586@bit.edu.cn (Q.X.); 3120200598@bit.edu.cn (M.Z.); 3120200533@bit.edu.cn (W.H.)

[2] Metrological Observation Centre of the China Meteorological Administration (CMA), Beijing 100081, China; buzhichao@163.com

* Correspondence: tanws@bit.edu.cn

Abstract: The remote sensing of water clouds is useful for studying their spatial and temporal variations and constraining physical processes in climate and weather prediction models. However, radar-only detection provides inadequate information for the cloud droplet size distribution. Here, we propose a novel lookup-table method, which combines lidar (1064, 532 nm) and radar (8.6 mm) to retrieve profiles of cloud optical (backscatter coefficient and extinction coefficient) and microphysical properties (effective diameter and liquid water content). Through the iteration of the extinction-to-backscatter ratio, more continuous cloud optical characteristics can be obtained. Sensitivity analysis shows that a 10% error of the lidar constant will lead to a retrieval error of up to 30%. The algorithm performed precise capture of the ideal cloud signal at a specific height and at full height and the maximum relative error of the backscatter coefficients at 1064 nm and 532 nm were 6% and 4%, respectively. With the application of the algorithm in the two observation cases on single or multiple cloud layers, the results indicate that the microphysical properties mostly agree with the empirical radar measurements but are slightly different when larger particles cause signal changes of different extents. Consequently, the synergetic algorithm is capable of computing the cloud droplet size distribution. It provides continuous profiles of cloud optical properties and captures cloud microphysical properties well for water cloud studies.

Keywords: water cloud; radar; multiwavelength lidar; optical properties; microphysical properties

Citation: Zhang, Y.; Chen, S.; Tan, W.; Chen, S.; Chen, H.; Guo, P.; Sun, Z.; Hu, R.; Xu, Q.; Zhang, M.; et al. Retrieval of Water Cloud Optical and Microphysical Properties from Combined Multiwavelength Lidar and Radar Data. *Remote Sens.* **2021**, *13*, 4396. https://doi.org/10.3390/rs13214396

Academic Editor: Carmine Serio

Received: 12 September 2021
Accepted: 23 October 2021
Published: 31 October 2021

1. Introduction

In the atmosphere, clouds cover about 67% of the globe and play a critical role in regulating the energy budget of the Earth [1]. In particular, the optical and microphysical properties of water clouds affect their capability to absorb and scatter radiation, and this poses a major challenge leading to uncertainty in numerical weather forecasts and climate simulations [2,3]. Testing and improving parameterization schemes for cloud variations and physical processes requires knowledge of cloud properties [4,5]. Hence, the current techniques will be validated and new ones will be developed for retrieving water properties. One of the best ways to collect cloud properties is using aircraft-mounted in situ probes, which are able to perform measurements of cloud microphysical properties directly and accurately. This approach is hampered by the scarcity of aircraft measurements by volume and is temporally and spatially limited [6–8]. Therefore, some active sensors are used alone or combined to generate a large amount of observational information about cloud characteristics [9,10]. Radar remote sensing is routinely operated from ground-based observations [11,12] and a variety of ship-based and satellite platforms [13,14]. Some radar-based studies use the empirical power-law relations between radar reflectivity factor

(Z) to liquid water content (LWC) or Z to effective diameter (D_{eff}) for retrieval cloud microphysical properties [6,15,16]. These empirical coefficients have been validated in the course of several national and international field experiments: the Cloud Lidar and Radar Experiment (CLARE'98) [15], Atlantic Stratocumulus Transition Experiment (ASTEX) [16], etc. However, radar cross section is proportional to the sixth power of the particle diameter D, and thus they are dominated by the largest particles in a volume and have a lower sensitivity to the smallest particles. It is difficult to use single-frequency radar to adjust to varied size distributions, as the empirical relations restrict the detection of samples with a distribution composed of small particles. Hence, completing droplet size distribution (DSD) plays an important role in observing the microphysical properties of clouds.

The radar–radiometer synergetic method can estimate the parameters of DSD and provide more accurate microphysical characteristics than radar-only measurements. The approach is to parameterize DSD by a lognormal functional form that can be characterized using three independent parameters (the cloud number concentration N_0, the logarithmic distribution σ, and the median diameter D_{log}). Since Z, LWC, and D_{eff} are affected by σ and D_{log} simultaneously, assuming a fixed value of σ can simplify the algebraic relationship to the Z-LWC or Z-D_{eff} [8,17,18]. A limitation to this method is that it requires assumptions of at least one of the DSD parameters, so this estimation method needs to be further strengthened.

The combination of lidar and radar measurements can also achieve more accurate measurements of cloud microphysical properties [19,20]. Since lidar has a shorter wavelength and is more sensitive to small particles, the lidar and radar complement each other by representing small and large particles in DSD. The most basic approach is to use the Z, lidar extinction coefficient (α) or backscatter coefficient (β) to define the characteristic droplet diameter that represents the ratio of radar reflectivity to the lidar extinction (Z/α) and the ratio of radar reflectivity to the lidar backscatter (Z/β). Afterward, the statistic distribution is used to construct the relations of characteristic droplet diameter to cloud microphysics (LWC and D_{eff}) [21]. Nevertheless, accurate inversion of α or β is one of the problems for single wavelength elastic lidar data. The Klett-type inversion method [21] can obtain α for cloud profiles when an α at a reference height is known in advance. Okamoto [22] presents a forward algorithm that corrects α and β without considering the far end value of the elastic signal, but it assumes a constant parameter σ of the DSD. Furthermore, recent studies illustrate that high spectral resolution lidar (HSRL) can retrieve cloud optical properties using the Z/β–LWC relations without any assumptions [10]. However, it is does not propose the method to completely determine all the parameters (N_0, σ, D_{log}) of the DSD.

According to the studies mentioned above, acquiring cloud optical and microphysical parameters from remote sensing observations is limited to the following: (i) restricts the retrievals for samples with empirical relationships especially for small particles; (ii) requires assumptions of at least one of the DSD parameters; and (iii) has large uncertainty of the α and β parameters of lidar inversion. In this paper, we present a retrieval technique for combined multiwavelength lidar and radar observations to determine all the parameters of the DSD. Through the implementation of the algorithm for ideal clouds and observation cases, it improves the continuous optical properties and performs well when capturing microphysical properties for water cloud studies.

The paper is structured as follows. All parameters introduced in this technique are defined in Section 2.1. Section 2.2 briefly describes the implementation of the algorithm, establishes a theoretical backscatter statistical model (BSM), and analyzes the sensitivity of the algorithm. The results of the application to the ideal cloud signal and observation cases are presented in Sections 3.1 and 3.2. Section 4 summarizes the paper.

2. Materials and Methods

2.1. Parameter Definitions

In this section, we briefly introduce the relationship between the lidar and radar observables and the cloud optical properties and microphysical properties from the per-

spective of DSD. Introducing the definitions of the lidar and radar equations, backscatter coefficient, extinction coefficient, lidar and radar ratio, LWC, and D_{eff} will aid us in explaining the combined lidar–radar algorithm.

The lidar and radar equations can be written in the same form [23,24]:

$$P(\lambda_{L,R}, z) = \frac{C_{L,R}}{z^2}\beta_t(\lambda_{L,R}, z)\exp\left(-2\int_0^{\infty}\alpha_t(\lambda_{L,R}, z)dz\right) \quad (1)$$

where the subscripts of L and R represent lidar and radar. P is the received power detected at the wavelength of λ_L and λ_R. $C_{L,R}$ is the constant that takes into account the instrument parameters. $\beta_t(\lambda_{L,R},z)$ and α_t $(\lambda_{L,R},z)$ are the total backscatter coefficients and extinction coefficients from the instrument to distance z.

Although the principles of lidar and radar are similar, radar signals are most commonly specified in terms of the radar reflectivity factor Z in Equation (2). The backscatter coefficient β_t (λ_R,z) can be calculated by Z and then converted into the form of Equation (1). K_w is calculated by the refractive index of water at the radar wavelength [21]:

$$Z(\lambda_R, z) = \frac{{\lambda_R}^4}{\pi^5|K_w|^2}4\pi\beta_t(\lambda_R, z) \quad (2)$$

The mentioned total extinction and backscatter coefficients consist of molecules and particles. In this study, we mainly focus on the extinction and backscatter for cloud particles that are defined as $\beta_p(\lambda_{L,R})$ and $\alpha_p(\lambda_{L,R})$ and are presented in Equations (3) and (4) [25]:

$$\beta_p(\lambda_{L,R}) = \int_0^{\infty}\sigma_b(D, \lambda_{L,R})\cdot n(D)dD = \frac{\pi}{4}\int_0^{\infty}Q_b(D, \lambda_{L,R})\cdot n(D)D^2dD \quad (3)$$

$$\alpha_p(\lambda_{L,R}) = \int_0^{\infty}\sigma_{ext}(D, \lambda_{L,R})\cdot n(D)dD = \frac{\pi}{4}\int_0^{\infty}Q_{ext}(D, \lambda_{L,R})\cdot n(D)D^2dD \quad (4)$$

The σ_b and σ_{ext} are backscatter and extinction scattering cross-sections and $n(D)$ is the DSD of the cloud particles. As Equations (3) and (4) show, the σ_b is a function of the Mie backscattering efficiency Q_b and particle diameter D. Similarly, the σ_{ext} is a function of the Mie extinction efficiency Q_{ext} and D.

The relationship between $\alpha_p(\lambda_{L,R})$ and $\beta_p(\lambda_{L,R})$ is defined by the extinction-to-backscatter ratio, which is the lidar ratio (LR_λ) [23]. Analogous to the definition of the LR_λ, we defined the radar ratio (RR) as:

$$LR_\lambda / RR = \frac{\alpha_p(\lambda_{L,R})}{\beta_p(\lambda_{L,R})} \quad (5)$$

To model the DSD of water clouds, we chose lognormal distribution as the function form of the DSD. The literature shows that the lognormal distribution function can be used to approximate empirical water cloud DSD [26,27]. Therefore, the cloud droplet size distribution $n(D)$ is given by Equation (6):

$$n(D) = \frac{N_0}{\sqrt{2\pi}\sigma D}\exp\left(\frac{-\ln\left(D/D_{\log}\right)^2}{2\sigma^2}\right) \quad (6)$$

The $n(D)$ is characterized by the cloud number concentration N_0, the dispersion parameter of the logarithmic distribution σ, and the median diameter D_{log}.

Through the parameterized DSD, the microphysical properties of the cloud, especially the LWC and D_{eff}, can be given in terms of the moment of the DSD using Equations (7) and (8) [20] as follows, where ρ_w is the density of water, and the angle brackets denote averaging over the size distribution.

$$\mathrm{LWC} = \frac{\pi}{6}\rho_w\int_0^{\infty}n(D)D^3dD = \frac{\pi}{6}\rho_w\left\langle D^3\right\rangle \quad (7)$$

$$D_{eff} = \frac{\int_0^\infty n(D)D^3 dD}{\int_0^\infty n(D)D^2 dD} = \frac{\langle D^3 \rangle}{\langle D^2 \rangle} \quad (8)$$

2.2. Implementation of the Algorithm

2.2.1. Overview

The implementation of the lidar–radar synergetic algorithm incorporates three observables—the radar reflectivity factor Z and the lidar signals at wavelengths of 1064 nm and 532 nm, P_{1064} and P_{532}. It mainly consists of five steps: data interpolation, cloud detection, optical retrieval, microphysical retrieval, and LR_λ/RR iteration. The schematic of the algorithm is expressed in Figure 1 and explained below.

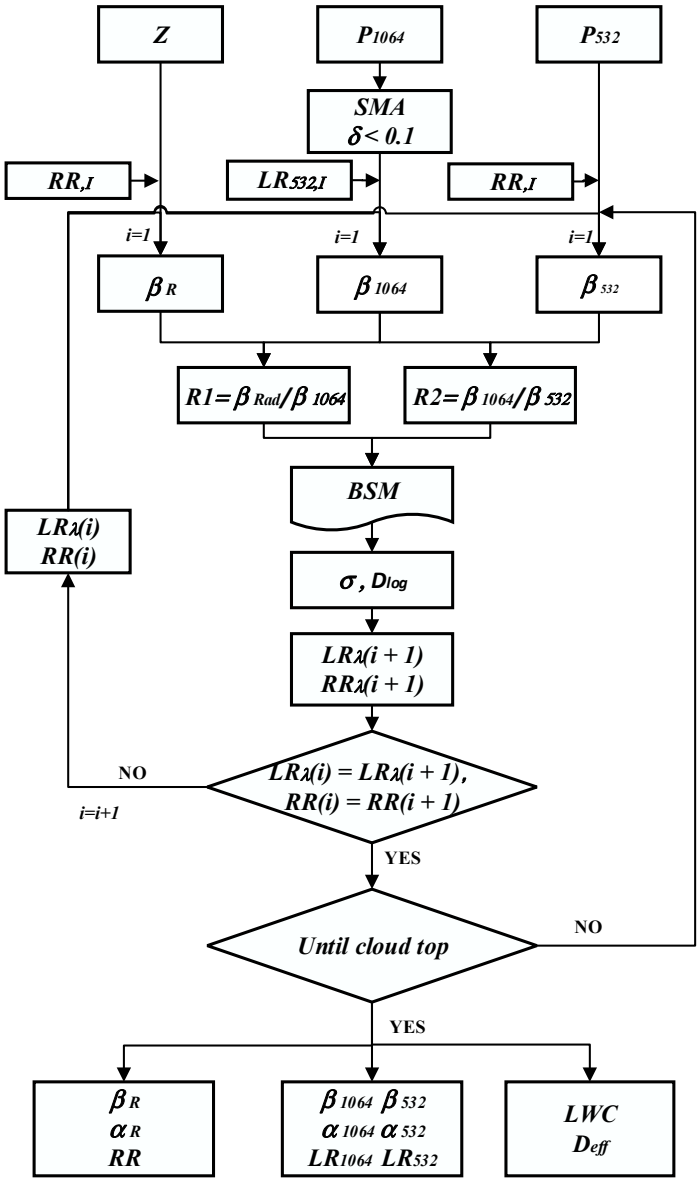

Figure 1. Schematic of the algorithm for the retrieval of optical and microphysical properties of clouds by multiwavelength lidar and cloud radar.

Firstly, lidar and radar data are averaged to the same time and range resolution. In this study, the range resolution and the time resolution are set to 30 m and 10 min, respectively.

Layers of clouds are then identified from the lidar and radar overlap region. Due to the distinguished ability of lidar to capture cloud bases, we use a simple multiscale

algorithm (SMA) [28] for cloud masking detection. Afterward, layers with a volume linear depolarization ratio (δ) at 1064 nm of less than 0.1 are selected as water cloud layers [29]. The range is recorded from the cloud base to the top.

Next, backscatter coefficients of clouds at lidar and radar wavelengths are retrieved by the Fernald forward integral method [30]. This algorithm uses pre-calibrated lidar constants and does not require the assumption of the backscatter coefficient at the reference height, thereby reducing the uncertainty of the inversion. The initial value of the lidar ratio ($LR_{\lambda,I}$) and radar ratio ($RR_{,I}$) need to be assumed before obtaining β at the beginning. The detailed methods to retrieve lidar/radar backscatter coefficients and lidar constant are supplied in Appendix A.

After deriving β for cloud particles at three wavelengths, two backscatter ratios, R1 = β_R/β_{1064} and R2 = β_{1064}/β_{532}, are defined for cloud microphysical property retrieval. A look-up backscatter statistical model (BSM) has been established through electromagnetic simulations to bridge the gap between the optical and microphysical properties. The DSD parameters, D_{log} and σ, can be looked up in BSM with the pairwise ratio R1 and R2 as inputs. The details of the BSM are introduced in Section 2.2.2.

Once D_{log} and σ are derived, LR_λ and RR can be calculated theoretically with the retrieved DSD. If the differences between the newly calculated and the previously used LR_λ/RR exceed the thresholds, the newly calculated LR_λ and RR are used to retrieve β and the subsequent DSD until the LR_λ and RR are stable at this height. After looping the iterative process from the cloud base to the cloud top, the profiles of cloud optical and microphysical properties can be retrieved eventually.

2.2.2. Backscatter Statistic Model (BSM)

In this section, we propose a BSM that aims to transfer cloud optical properties to microphysical properties and validate the accuracy of the model. In detail, we first calculate the backscatter coefficient based on nature's DSD distribution. Then, we establish a model relationship between the backscatter coefficient and parameters of DSD (D_{log} and σ). Finally, we confirm the accuracy of the BSM.

The theoretical calculations of the particle backscatter coefficients β_R, β_{1064}, and β_{532} is achieved using Mie theory. Since only cloud droplets are considered in this research, the particle shape is assumed to be spherical. The range of droplet diameters D is assumed to be 0.5–100 μm for this study. $\beta_p\ (\lambda_{L,R})$ and $\alpha_p\ (\lambda_{L,R})$ can be calculated using Equations (3) and (4). The parameters are defined below. The Q_{ext} *and* Q_b are also implicit functions of the refractive index of water. The refractive index of water clouds at 20 °C at the wavelengths 532 nm, 1064 nm, and 8.6 mm are 1.33–j(1.32×10^{-9}), 1.32–j(2.89×10^{-6}), and 5.25–j(2.81), respectively [31,32].

As for the range of the parameters (N_0, D_{log}, σ) of $n(D)$, they are set to be N_0 = 200 cm^{-3}, $0.1035 \leq \sigma \leq 0.8$, and $0.3 \leq D_{log} \leq 66.7$ μm, which are converted by a series of observations [14,33–35]. Figure 2a shows the backscatter cross section for each wavelength using the above parameters. The relation of the LR_λ/RR with the D_{eff} is shown in Figure 2b. The single-colored lines represent the condition of the same D_{log} but different σ values. The parameters of DSD lead to a rapid change in LR_λ/RR and present a unique trend in LR_λ/RR along with the D_{eff}. Admittedly, the LR_λ and RR can characterize the changes in the cloud's microphysical properties.

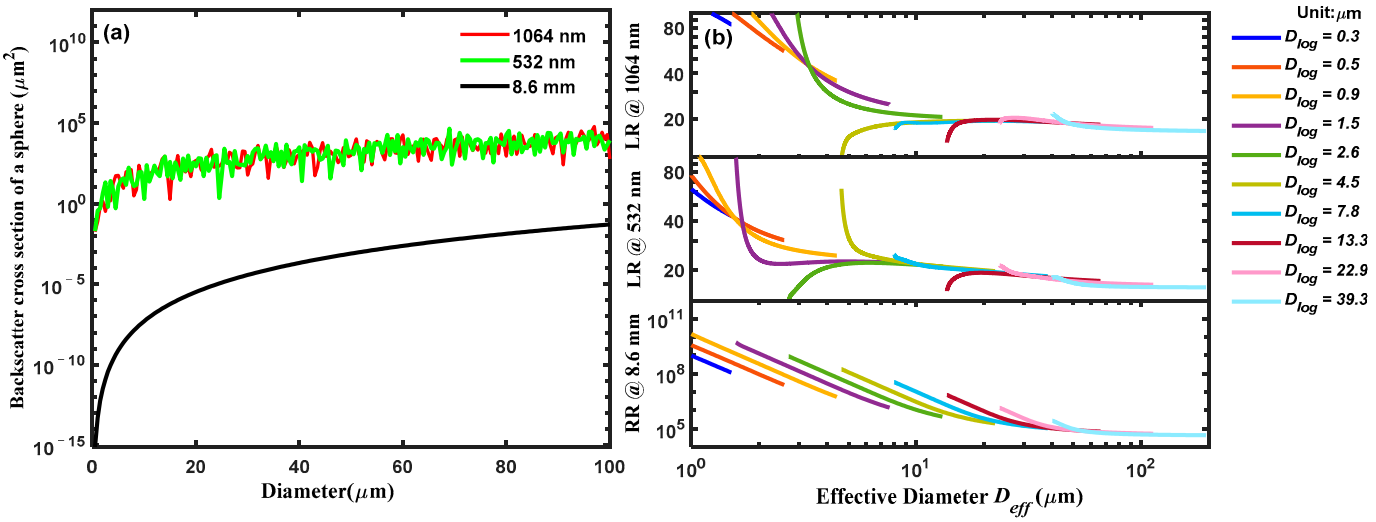

Figure 2. (**a**) The backscatter cross section of lidar at 532 nm (green) and 1064 nm (red), and radar at 8.6 mm (black); (**b**) The relations between lidar ratio (LR_λ) and radar ratio (RR) with effective diameter.

After the theoretical calculation of the optical properties from the microphysical properties, how to convert the optical properties to microphysical properties is the main problem due to there being no algebraical formula describing these relationships with DSD known in advance. Therefore, we calculate the backscattering through theoretical simulation and construct a statistical table to assess the relationship between β and DSD. Because three variables influence the DSD, we determine the R1 and R2 when ignoring the influence of N_0 in the algorithm. The range of R1 and R2 differ by several orders of magnitude, hence they are set at exponential and linear intervals, respectively. The center median of D_{log} and σ is calculated using Equation (9) as the final value for each interval

$$\overline{X} = \sum_{i=1}^{N} \frac{Xi}{N} \tag{9}$$

where N is the numbers of parameters in the specific interval, and Xi are the parameters in that interval. Finally, the BSM has been organized as shown in Figure 3.

Figure 3a shows that the D_{log} has a proportional relationship with R1 when R2 is constant. On the contrary, σ exhibits a complex relationship between R1 and R2. Thus, constructing the BSM can easily yield the sophisticated DSD based on R1 and R2. The standard deviation of the D_{log} and σ is shown in Figure 3c,d. The large deviation between the two shows the uncertainty between the model values and the real parameters.

To evaluate the accuracy of the BSM, we compared the look-up BSM results to simulation results (SIM). The four microphysical parameters are located at the 1:1 line (black line) in Figure 4. The correlation coefficients (R^2) for σ, D_{log}, D_{eff}, and LWC are 0.89, 0.97, 0.96, and 0.87, respectively. Other metrics, such as the Nash–Sutcliffe efficiency (NSE) [36], measure how well predictions are relative to the observed average. The NSE for D_{log}, σ, D_{eff}, and LWC are 0.94, 0.78, 0.94, and 0.72, respectively. RMSE standard deviation ratio (RSR) is defined as the standardized RMSE using the simulations' standard deviations, which makes all variables comparable. The RSR for D_{log}, σ, D_{eff}, and LWC are 0.47, 0.25, 0.29, and 0.53, respectively. Among all the parameters, the D_{log} and D_{eff} show the best fit to the model, and the smallest deviation belongs to σ and D_{eff}. In summary, all the parameters of BSM highlight its great performance for the conversion of optical to microphysical properties.

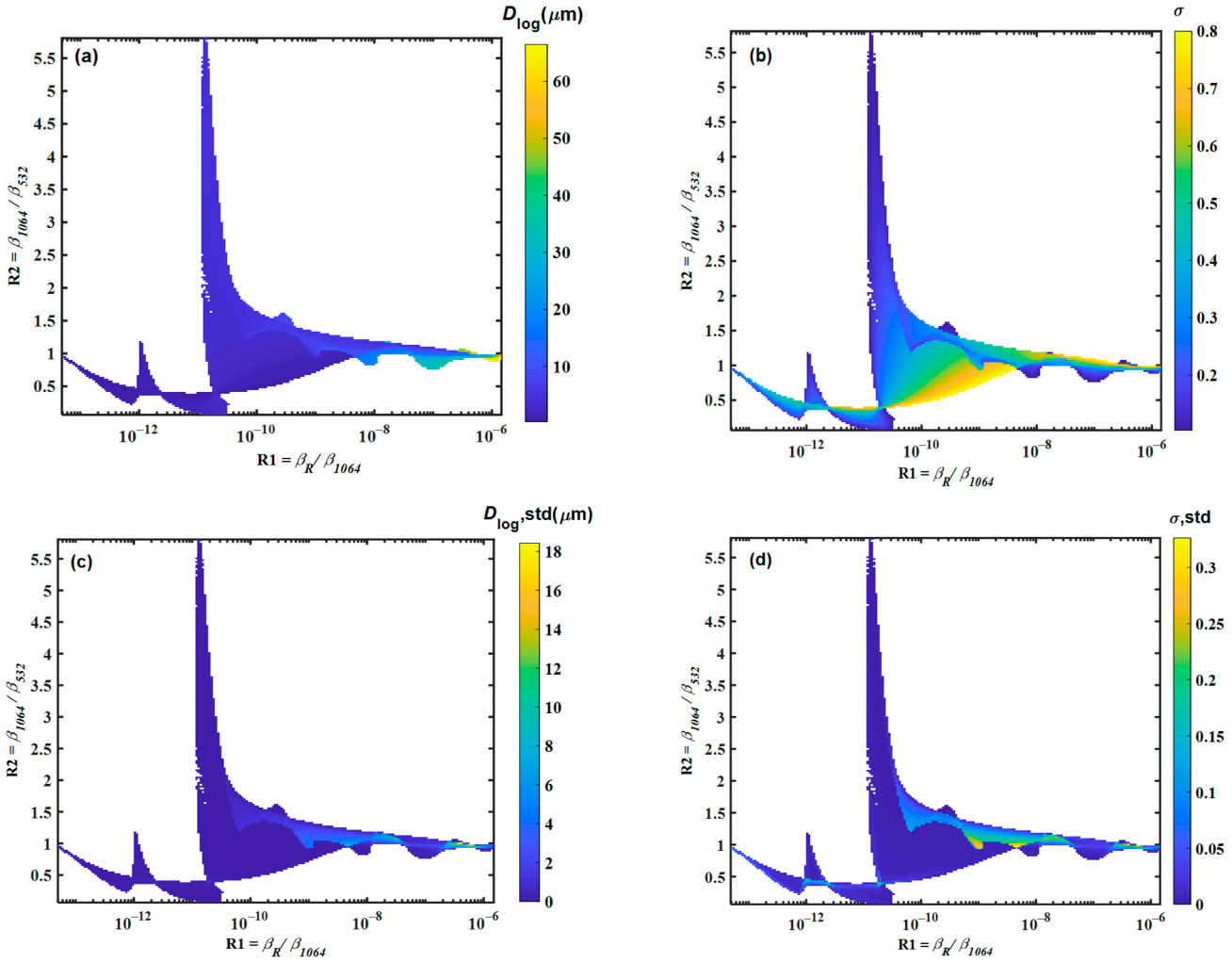

Figure 3. (**a**) The backscatter statistical model for median diameter (D_{log}); (**b**) the backscatter statistical model for logarithmic width of the distribution (σ); (**c**) the standard deviation of the D_{log} (D_{log}, *std*) in the backscatter statistical model; (**d**) the standard deviation of σ (σ, *std*) in the backscatter statistical model.

2.2.3. Sensitivity Analysis

Considering the robustness of the inversion results, we analyze the sensitivity of the initial value of lidar/radar ratio ($LR_{532,I}$ $LR_{1064,I}$ $RR_{,I}$) and the instrument constant (C_{532}, C_{1064}, C_{rad}) to the uncertainty of the lidar/radar ratio (LR_{532}, LR_{1064}, RR), backscatter coefficient (β_{532}, β_{1064}), radar reflectivity (Z), and microphysical properties (D_{eff}, LWC).

We assumed the parameters of DSD with a typical water cloud condition [34]. The change range for the initial value of lidar/radar ratio and instrument constant are set between ±30% and ±10%, individually. The maximum relative error induced by the $LR_{\lambda,I}$ and $RR_{,I}$ is less than 1%, so the error of these input parameters can be ignored. The sensitive test for the instrument constant is shown in Figure 5. As Figure 5a,b shows, the lidar constant (C_{532}, C_{1064}) has a more significant impact on microphysical properties than the radar constant (C_{rad}), especially for the C_{532} where a 10% error results in a retrieval error of up to 30%. Therefore, a cautious restriction for the error of lidar constant should be considered.

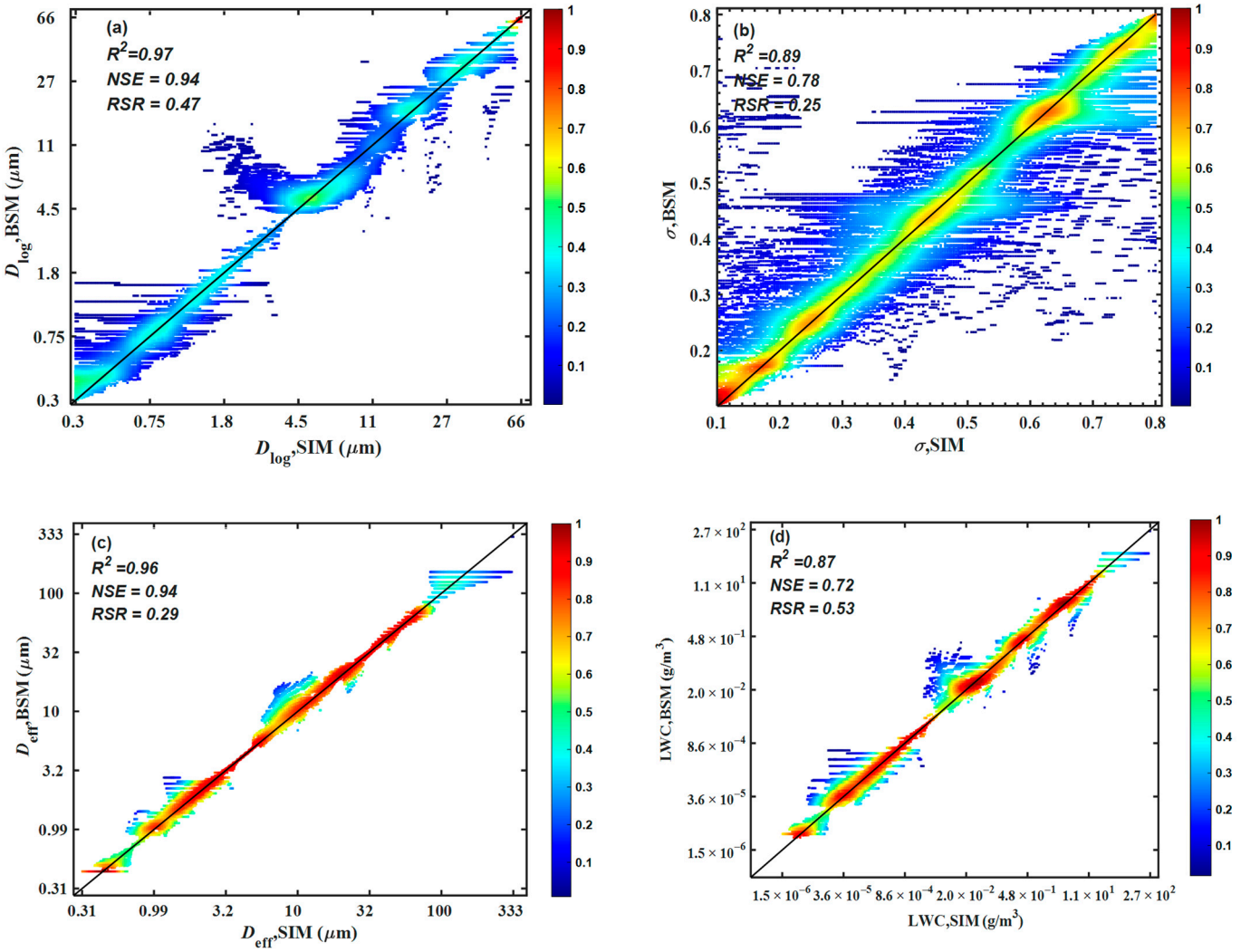

Figure 4. Comparison of the results of the look-up backscatter statistical model (BSM) with simulation results (SIM). The solid black line is the 1:1 line, the color bar represents the normalized density of the data: (**a**) the median diameter (D_{log}); (**b**) the logarithmic width of the distribution (σ); (**c**) the effective diameter (D_{eff}); and (**d**) the liquid water content (LWC).

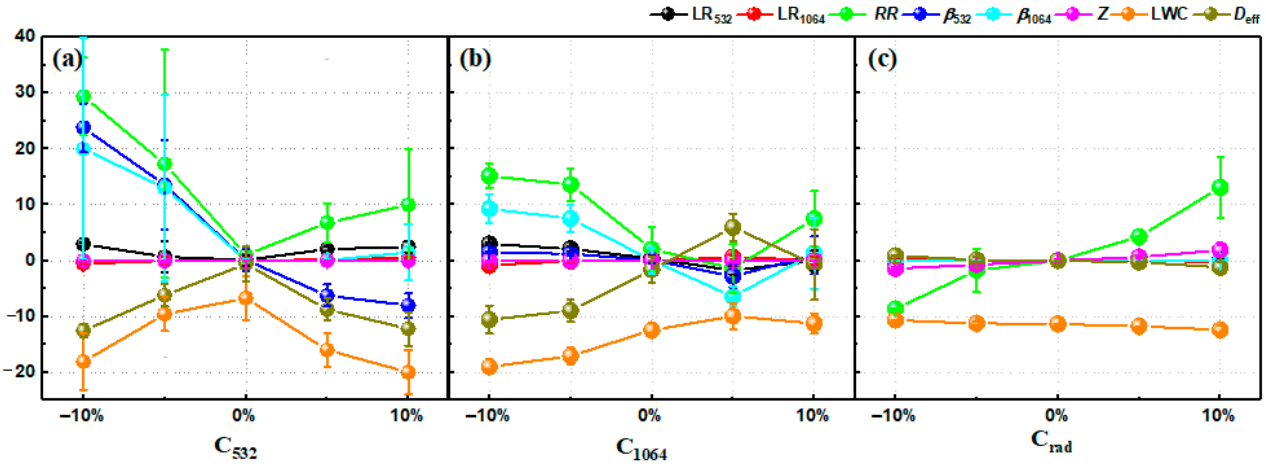

Figure 5. Results for the relative error with changes in the initial parameters: (**a**) lidar constant at 532 nm (C_{532}); (**b**) lidar constant at 1064 nm (C_{1064}); (**c**) radar constant (C_{rad}).

3. Results and Discussion

3.1. Application to the Ideal Cloud Signal

The feasibility and stability of the algorithm had been proven in preliminary testing. We simulated the ideal cloud signal to verify the inversion results at a specific height and at full height. Here, we used a thin cloud located from 3 to 3.3 km with a lognormal DSD of water particles as our example. With the implementation of the look-up BSM, the LR_λ and RR iteration at cloud base is shown in Figure 6. The inversion results for full height are shown in Figures 7 and 8.

The iteration results with the fixed D_{log} and σ at cloud base are shown in Figure 6. The initial values of lidar/radar ratio were set as 20, 15, and 10^6 for $LR_{532,I}$, $LR_{1064,I}$, and $RR_{,I}$, respectively. It can be seen in Figure 6a that the LR_λ and RR were stable after three iterations. Similar results were shown for the larger particles. The iteration was stopped for lookup BSM twice (Figure 6b).

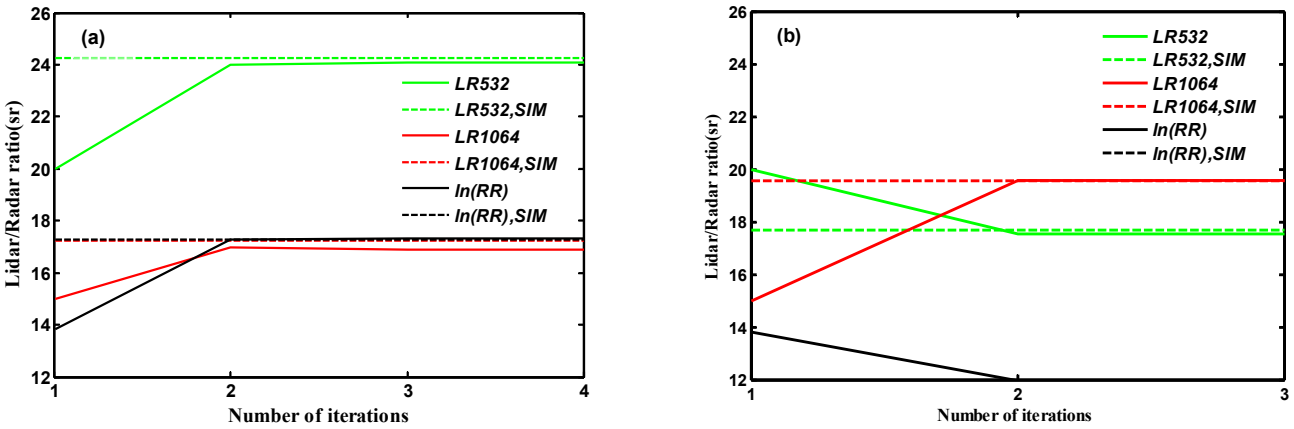

Figure 6. The iteration results for the lidar ratio (LR)/radar ratio (RR) at a fixed altitude. The ln(RR) indicates the natural logarithm of RR. The inversion (solid line) and the simulated value (SIM, dash line) results assumed the median diameter (D_{log}) and the width of the distribution (σ): (**a**) D_{log} = 7.7 μm, σ = 0.38; (**b**) D_{log} = 35 μm, σ = 0.4.

The full height inversion results of cloud properties, such as LR_λ, RR, β_{532}, β_{1064}, Z, LWC, and D_{eff}, are shown in Figures 7 and 8. Compared with the simulation results (SIM, dotted lines), the retrieved values were approximate to the true values for the whole cloud layer.

For optical properties, the LR_λ/RR results were similar to the simulation for different parameters of DSD (Figures 7a,b and 8a,b). Compared to the result assuming constant $LR_{\lambda,I}/RR_I$ for $\beta_{\lambda,I}$ and $Z_{,I}$ profile, the results after iteration showed a significant change for β_λ and Z in profile. Especially for Figure 8c, the algorithm showed a better ability to capture complete profiles and improved the detection capability of lidar. The maximum relative error of the backscatter coefficient in profiles is 4% and 6% for β_{1064} and β_{532}, respectively.

The performance of the microphysical property retrieval depends on nature's conditions. The results were compared with a series of empirical formulas for LWC, which was attached to Atlas [37], Fox [16], and Baedi [15]. Likewise, the D_{eff} was attached to Atlas, Continent (C) [34], and Marine (M) [34] as stipulated in the literature. Figure 7d,e shows that the retrieved LWC and D_{eff} were located between the empirical formula Z-LWC and Z-D_{eff}. However, a large deviation between the LWC and D_{eff} occurred in Figure 8d,e due to the presence of large particles. It should be emphasized that when only a small number of large particles are present, the contribution of the LWC and D_{eff} as determined by Z could be challenging.

3.2. Application to Lidar and Radar Observation

In this section, the newly proposed algorithm was applied to the observation of a water cloud using lidar with 532 nm, 1064 nm, and cloud radar with 8.6 mm. These

two instruments are collocated at the Haidian meteorological station, Beijing, China (39.983°N 116.283°E). The 60-day observation campaign was from September 2019 to October 2019. The technical specification of the lidar was used in Wang's studies [15]. The cloud radar was produced by the Meteorological Observation Center of the China Meteorological Administration and Huateng Microwave Co. Ltd. Radar provided measurements of the reflectivity (Z), mean Doppler velocity (V_D), and Doppler spectrum width (W_D). It operated continuously in meteorological stations [38]. The Chinese Academy of Meteorological Sciences (CAMS) AERONET station (39.933°N 116.317°E) was used to calibrate the lidar constant, which was at a distance of 3 km from the observation stations.

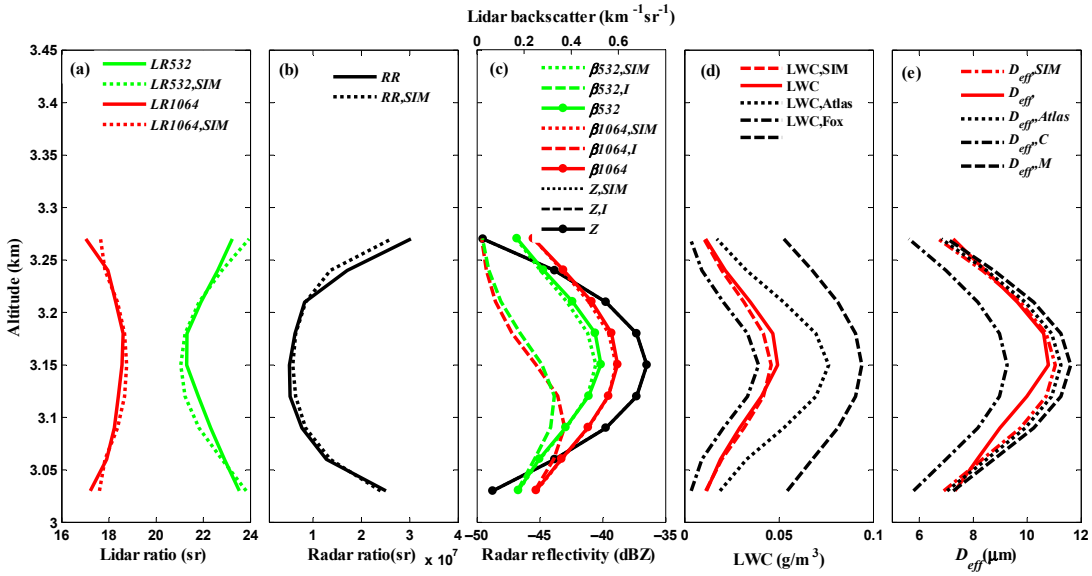

Figure 7. Comparison of the iteration results (solid line) with the simulation (SIM, dot line) in profile. The DSD parameter was the same as in Figure 6a: (**a**) lidar ratio at different wavelengths (LR_{532}, LR_{1064}); (**b**) radar ratio (RR); (**c**) lidar backscatter at different wavelengths (β_{532}, β_{1064}) and radar reflectivity factor (Z) (initial value subscript I, dash line); the results of different Z were superimposed. (**d**) Liquid water content (LWC); (**e**) effective diameter (D_{eff}).

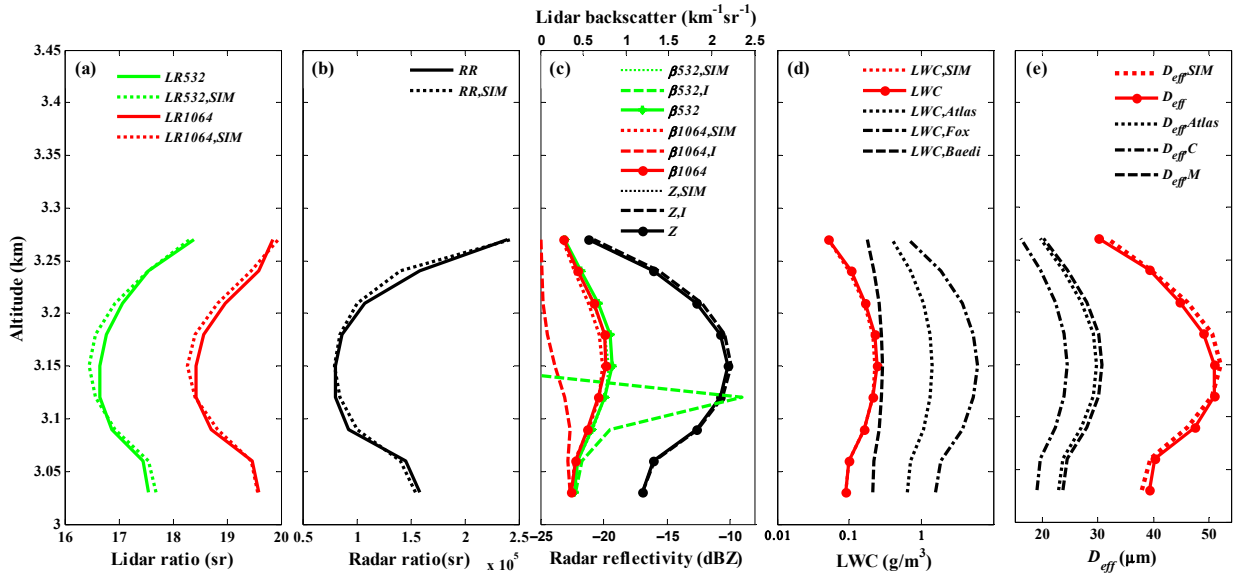

Figure 8. Comparison of the iteration results (solid line) with the simulation (SIM, dot line) in profile. The DSD parameter was the same as in Figure 6b: (**a**) lidar ratio at different wavelengths (LR_{532}, LR_{1064}); (**b**) radar ratio (RR); (**c**) lidar backscatter at different wavelengths (β_{532}, β_{1064}) and radar reflectivity factor (Z) (initial value subscript I, dash line); the β_{532}, SIM was superimposed in β_{532} (**d**) liquid water content (LWC); (**e**) effective diameter (D_{eff}).

3.2.1. Observation in a Layer of the Cloud

Figure 9 shows the time height profile for radar reflectivity (Z) and 1064 nm lidar ranged-correct signal (RCS) on October 10, 2019. There was a water cloud 3 km above ground between 00:00–10:00 local standard time (LST). Two moments at 2:30 a.m. and 4 a.m. were selected to show the results of the inversion.

At 2:30 a.m. (Figure 10), the LR_λ and RR had significant changes in the same region, and the β and Z rose to the same range. The algorithm had a significant effect on the lidar retrieval, which was calibrated using the β from the initial value (Figure 10c). It has the same effect as the simulation mentioned above. Compared with the microphysical retrieval, results were close to Baedi's LWC and Marine's D_{eff} at most heights. A difference appeared at the height of 3.9–4.5 km, where Z increased rapidly and β increased slowly, indicating the existence of large particles, which is verified in Figure 10e. Another difference can be seen at a height of 5–6 km, with the instantaneous decrease in Z and a nearly unchanged β. As a result of the decreased R1 and the fixed R2 for BSM, the lookup-table value of D_{log} was reduced.

At 4 a.m. (Figure 11), the LR_λ/RR changed with almost the same trend. Figure 11c shows that the Z and β contributed to the same range but to different extents. Specifically, lidar was more sensitive at a height of 4–4.6 km, while radar changed rapidly at all other heights. The results in Figure 11e verified this condition. The D_{eff} was relatively small at low altitudes and larger at the top, which caused a large deviation between the empirical relations. The LWC was smaller than the unique Z-LWC relations at this moment because the large particles contribute less to the LWC.

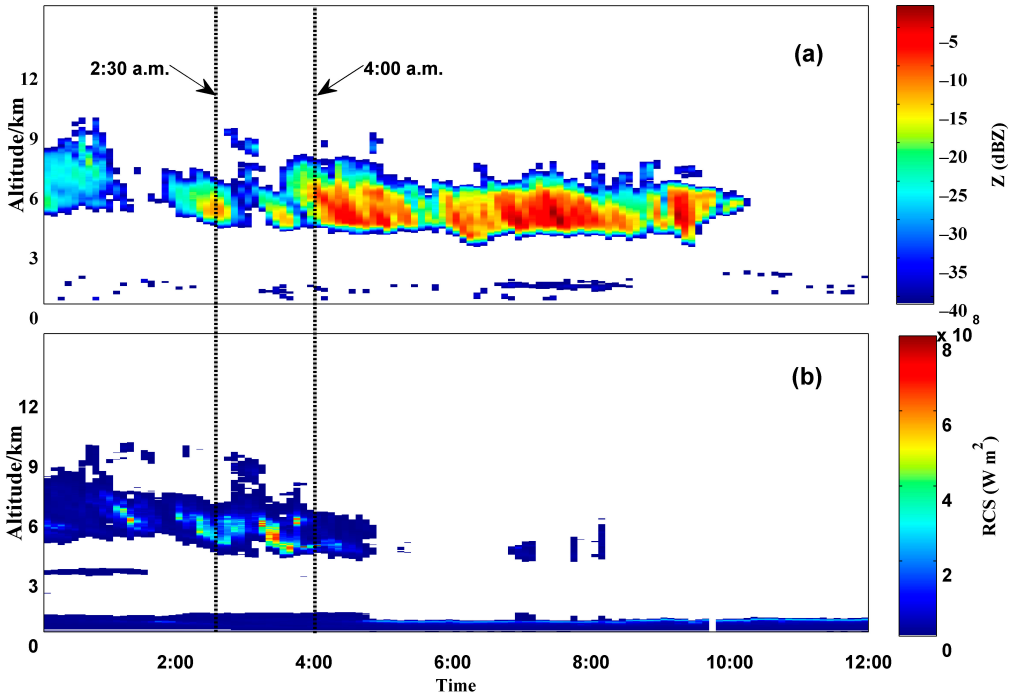

Figure 9. Time–height profile of Z (**a**) and 1064 nm ranged corrected signal (RCS) (**b**) on 10 October 2019.

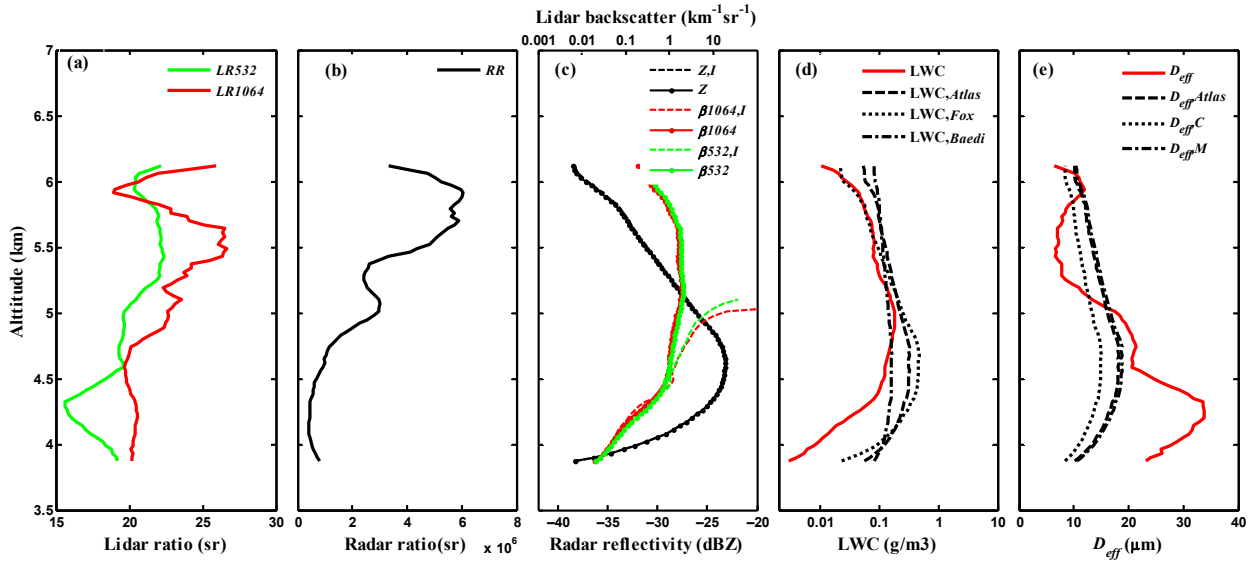

Figure 10. The inversion results at 2:30 am on 10 October 2019: (**a**) lidar ratio at different wavelengths (LR_{532}, LR_{1064}); (**b**) radar ratio (*RR*); (**c**) lidar backscatter at different wavelengths (β_{532}, β_{1064}) and radar reflectivity factor (*Z*) (initial value subscript *I*); (**d**) liquid water content (LWC); (**e**) effective diameter (D_{eff}).

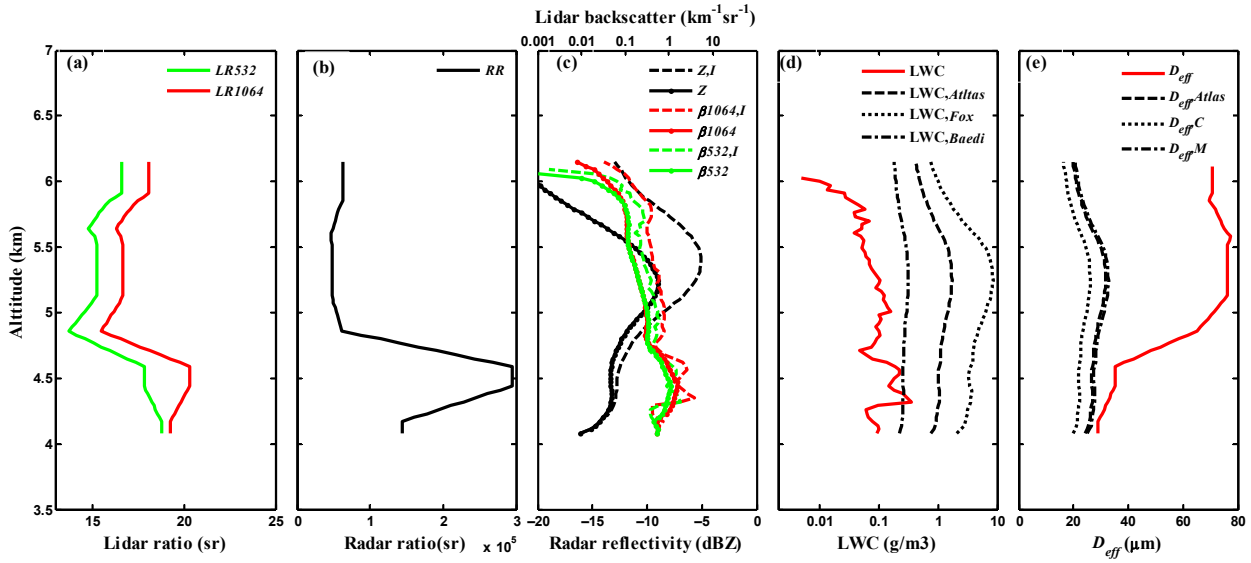

Figure 11. The inversion results at 4:00 a.m. on 10 October 2019: (**a**) lidar ratio at different wavelengths (LR_{532}, LR_{1064}); (**b**) radar ratio (*RR*); (**c**) lidar backscatter at different wavelengths (β_{532}, β_{1064}) and radar reflectivity factor (*Z*) (initial value subscript *I*); (**d**) liquid water content (LWC); (**e**) effective diameter (D_{eff}).

3.2.2. Observation in Multiple Layers of the Cloud

Figure 12 shows the time height profile for *Z* and *RCS* on 16 October 2019. A water cloud was 4 km above ground between 12:00 and 00:00 LST. The two moments at 13:00 and 20:30 were selected to observe the inversion results of multiple cloud layers.

At 13:00 (Figure 13), the LR_λ/RR had significantly changed in the same heights. Additionally, the rapid change of LR_λ/RR corresponds to the change of D_{eff} in the same region. The radar and lidar showed several peaks in the profile representing different DSD information. Notably, the lidar has a peak at 4.5 km, but with such peak in the radar data at the different height. This is evidence for the existence of a large number of small particles. The reduced D_{eff} at that height verified the observation in Figure 13e. The microphysical characteristic of LWC coincides with Fox's at 4.4 km but closer to Baedi's immediately above. The D_{eff} was close to the continent's D_{eff} at this moment. At 20:30 (Figure 14),

LR_λ/RR had significantly changed in a similar region. The radar showed a similar intensity at two layers, but the lidar had a smaller intensity at the lower one than the upper one (Figure 14c), suggesting that there is a larger D_{eff} at the top. This conclusion is supported by Figure 14e. The microphysical characteristic of LWC was close to Baedi's formula and Atlas's D_{eff} at this moment.

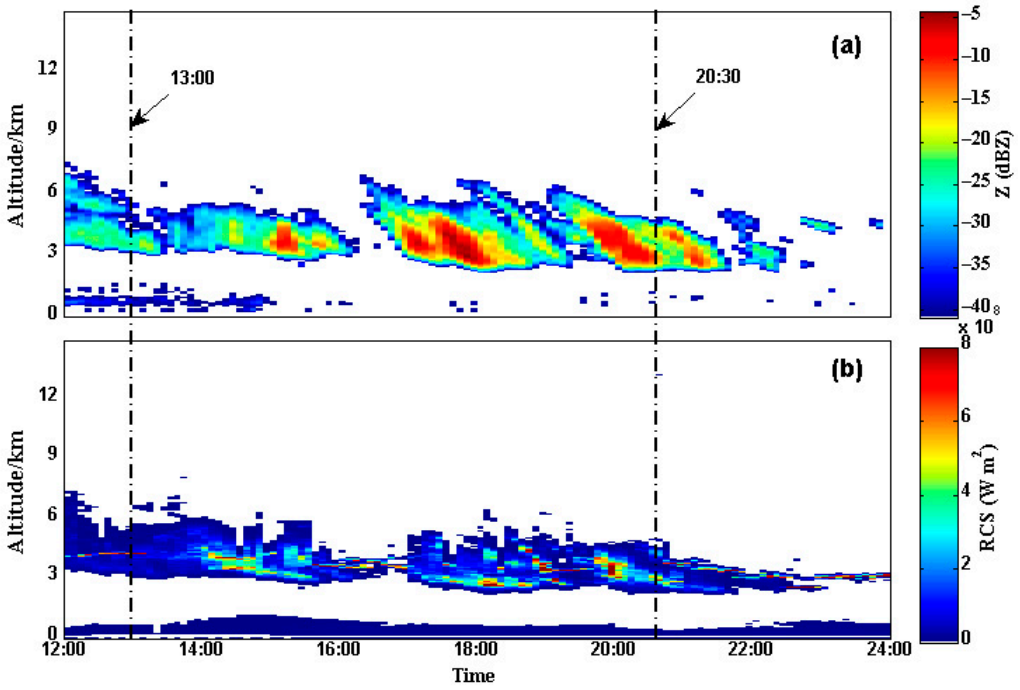

Figure 12. Time–height profile of Z (**a**) and 1064 nm ranged corrected signal (RCS) (**b**) on 16 October 2019.

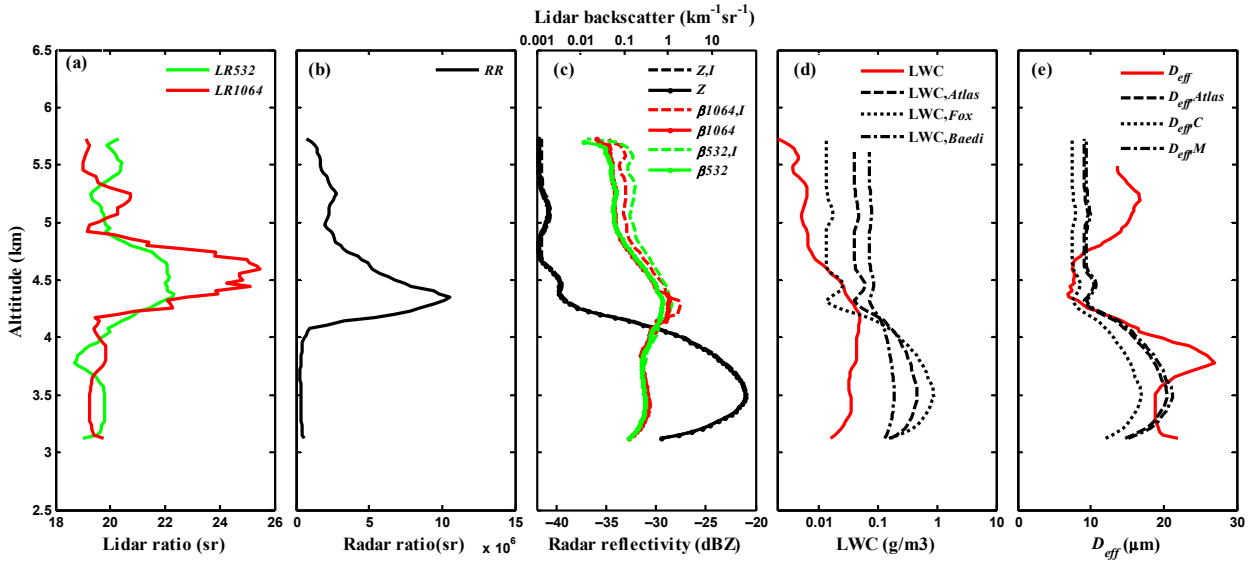

Figure 13. The inversion results at 13:00 p.m. on 16 October 2019: (**a**) lidar ratio at different wavelengths (LR_{532}, LR_{1064}); (**b**) radar ratio (RR); (**c**) lidar backscatter at different wavelengths (β_{532}, β_{1064}) and radar reflectivity factor (Z) (initial value subscript I); (**d**) liquid water content (LWC); (**e**) effective diameter (D_{eff}).

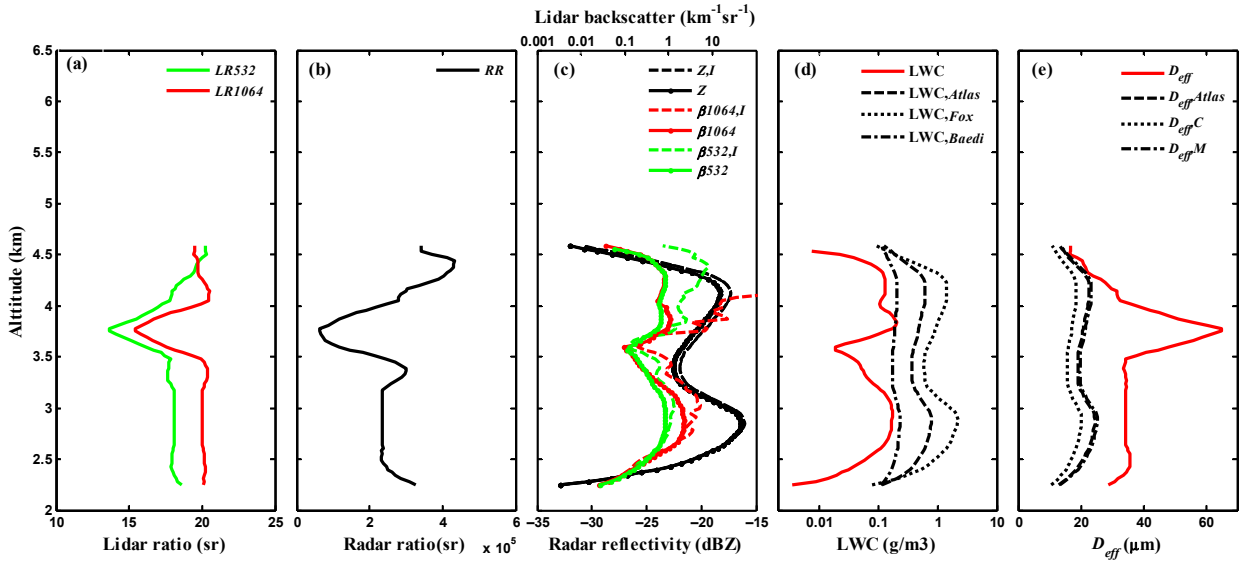

Figure 14. The inversion results at 20:30 p.m. on 16 October 2019: (**a**) lidar ratio at different wavelengths (LR_{532}, LR_{1064}); (**b**) radar ratio (RR); (**c**) lidar backscatter at different wavelengths (β_{532}, β_{1064}) and radar reflectivity factor (Z) (initial value subscript I); (**d**) liquid water content (LWC); (**e**) effective diameter (D_{eff}).

3.2.3. Strengths and Limitations of the Application of the Combination Algorithm to Observation Cases

The cloud radar is the most suitable instrument with which to observe clouds in day and nighttime. It shows the best continuity of the data and the complete data volume for all kinds of cloud layers. As for lidar, although it is very precise at detecting the cloud base, it cannot penetrate the thick optical depth cloud due to the attenuation of the beam in the cloud. Consequently, the limitation of the efficiency of the lidar–radar combining algorithm is restricted by the capability of lidar detection. Nevertheless, the lidar–radar algorithm has less data volume than the radar-only detection, and it advances atmospheric observation capabilities substantially. It is useful for the accurate detection of cloud optical and microphysical properties in further scientific research. In addition, the problem of the insufficient dataset can be complemented by a nearby wavelength radar system, for example, 95 GHz radar (3.2 mm).

4. Conclusions

Lidar and cloud radar are excellent instruments in the routine observation of temporal and spatial water cloud properties. Synergizing lidar and radar measurements of clouds advance atmospheric observation capabilities on many frontiers. We offer new insights on combined lidar (1064, 532 nm) and cloud radar (8.6 mm) to complete the three parameters of DSD, which is a long-standing dilemma in the observation of water clouds. The algorithm mainly consists of five parts: (a) data interpolation, (b) cloud detection, (c) optical retrieval, (d) microphysical retrieval, and (e) LR_λ/RR iteration. This algorithm proposes a forward technique to establish BSM to transfer the backscatter coefficient to the parameters of DSD.

The feasibility of the BSM is discussed in the simulation. The correlation coefficients (R^2) for σ, D_{log}, D_{eff}, and LWC are 0.89, 0.97, 0.96, and 0.87, respectively. The NSE for D_{log}, σ, D_{eff}, and LWC are 0.94, 0.78, 0.94, and 0.72, and the RSR are 0.47, 0.25, 0.29, and 0.53, respectively. This indicates that the D_{log} and D_{eff} show the best fit of the model and the smallest deviation belongs to σ and D_{eff}. All the parameters show the excellent performance for BSM to establish a model relationship between backscatter to clouds' microphysical variables. Through iteration of the extinction-to-backscatter ratio, the accuracy profiles of the optical properties and microphysical properties can be obtained. The features of the algorithm do not rely on the unique relationship of observations and can derive the LWC and D_{eff} in particular. Moreover, this method does not require an assumption about the

parameters (N_0, D_{log}, σ) of DSD and is applicable over a broad range of Z. In addition, the uncertainty of β has been improved by the iterative LR_λ/RR ratio. Consequently, these algorithms are more effective in observing continuous optical and precise microphysical properties in water clouds.

We performed a sensitivity test for the initial value of lidar/radar ratios ($LR_{532,I}$, $LR_{1064,I}$, $RR_{,I}$) and the instrument constant (C_{532}, C_{1064}, C_{rad}) to the uncertainty of the lidar/radar ratio (LR_{532}, LR_{1064}, RR), backscatter coefficient (β_{532}, β_{1064}), radar reflectivity (Z), and cloud microphysical properties (D_{eff}, LWC). Among these parameters, the lidar constant is the most sensitive in the test. This highlights the cautiousness necessary in constraining the error of the lidar constant (C_{532}, C_{1064}). Because the lidar constant can change slightly over time, we suggest using the same day or nearest day's lidar constant to reduce the error of the measurement.

Application to the ideal cloud signal shows that both iterations result in specific clouds and full heights. The iteration results for cloud bases show that both small particles and larger particles can approach stability after several iterations. The iteration results for the maximum relative error of the backscatter coefficient in profiles is 6% and 4% for β_{532} and β_{1064}, respectively. It improves the continuous lidar signal through the iteration of the lidar ratio. However, due to the presence of larger particles, the empirical relations are challenging.

The implementation of the algorithm in observation cases shows that the results of Z and β are proportional to D_{eff} and LWC in usual cases. However, the lidar supplies additional information for the complete DSD, which caused deviations in the empirical relationship of radar measurements. The synergetic algorithm shows an excellent ability to obtain cloud droplet spectrum information with a single peak or multiple peaks. Consequently, this technique can be developed in the observation of the cloud's spatial and temporal variations.

The limitation of the lidar–radar combined system requires only the lidar–radar overlap region, which means that the amount of efficiency in the dataset is smaller than the radar-only detection. This technique is important to supplement the DSD in principle and fill the gaps in this research field. In addition, the problem of an insufficient dataset can be complemented to combine other wavelength results of remote sensing instruments. Moreover, if the airborne probes could be observed instantaneously, this technique could be validated.

With the development of routine observations, observational stations have been installed at multiwavelength lidar and cloud radar stations for further scientific research. This algorithm could collect long-term water cloud properties and improve parameterization schemes for climate and weather prediction models.

Author Contributions: Conceptualization, Y.Z. and S.C. (Siying Chen); methodology and writing, S.C. (Su Chen) and W.T.; software, P.G.; project administration, H.C. and Z.B.; validation Z.S.; writing—review and editing, R.H., Q.X., M.Z. and W.H. All authors have read and agreed to the published version of the manuscript.

Funding: This research was funded by the China Postdoctoral Science Foundation (2020M680369).

Data Availability Statement: Data can be accessed by contacting Wangshu Tan (tanws@bit.edu.cn).

Acknowledgments: We wish to thank the China Meteorological Administration (CMA) for providing the lidar and radar data.

Conflicts of Interest: The authors declare no conflict of interest.

Appendix A

Appendix A.1. Retrieval Method of Lidar Backscatter

The lidar equation is shown in Equation (A1). Where P is the received power detected by wavelength lidar λ_L. C_L is the lidar constant. β_t and α_t are the total backscatter coefficients and extinction coefficients at range z, respectively.

$$P(\lambda_L, z) = \frac{C_L}{z^2}\beta_t(\lambda_L, z)\exp\left(-2\int_0^\infty \alpha_t(\lambda_L, z)dz'\right) \tag{A1}$$

The ranged corrected signal (RCS) is shown in Equation (A2).

$$RCS(\lambda_L, z) = C_L\beta_t(\lambda_L, z)\exp\left(-2\int_0^\infty \alpha_t(\lambda_L, z)dz'\right) \tag{A2}$$

Taking into account that the atmosphere consists of the aerosol and molecular components, which are represented by subscripts p and m, respectively, the total extinction and backscatter coefficient has to be written as Equation (A3):

$$\begin{array}{c}\alpha_t = \alpha_p + \alpha_{\mathrm{m}} \\ \beta_t = \beta_p + \beta_m\end{array} \tag{A3}$$

The extinction to backscatter ratio for particles and molecules LR_p and LR_m are shown in Equation (A4):

$$\begin{array}{c}\alpha_p = LR_p \times \beta_p \\ \alpha_m = LR_m \times \beta_m\end{array} \tag{A4}$$

Based on the Fernald type inversion, the backscatter coefficient can be expressed as Equation (A5):

$$\beta_p(\lambda_L, z) = \frac{RCS(\lambda_L, z)\exp\left(-2\int_0^\infty (LR_p(\lambda_L, z) - LR_m(\lambda_L, z))\beta_m(\lambda_L, z')dz'\right)}{C_L - 2\int_0^z LR_p(\lambda_L, z)RCS(\lambda_L, z)\exp\left(-2\int_0^\infty (LR_p(\lambda_L, z) - LR_m(\lambda_L, z))\beta_m(\lambda_L, z')dz'\right)dz} \tag{A5}$$

Since the error of the forward integration increases significantly with the detection distance z, we used the AOD, which is detected by the AERONET sites, to correct the aerosol below the cloud base. Thus, we can obtain a more accurate cloud backscattering coefficient. The optimized formula is shown in Equation (A6):

$$\beta_p(\lambda_L, z) = \frac{RCS(z,\lambda_L)\exp\left(-2\int_{z_b}^\infty (LR_p(\lambda_L,z) - LR_m(\lambda_L,z))\beta_m(\lambda_L,z')dz'\right)}{C_L\exp(-2AOD_{\lambda_L}) - 2\int_{z_b}^\infty LR_p(\lambda_L,z)RCS(z,\lambda_L)\exp\left(-2\int_{z_b}^z (LR_p(\lambda_L,z) - LR_m(\lambda_L,z))\beta_m(\lambda_L,z')dz'\right)dz} \tag{A6}$$

where z_b indicates the base of the cloud layer. Additionally, the $AOD_{\lambda L}$ is the aerosol optical depth at the corresponding wavelength λ_L.

Appendix A.2. Calibrate Lidar Constant C_L

As derived from Equation (A2), the lidar constant is transferred into the following form:

$$C_L = \frac{P(\lambda_L, z)z^2}{\beta_t(\lambda_L, z)\exp\left(-2\int_{z_0}^z \alpha_t(\lambda_L, z)dz'\right)} \tag{A7}$$

$$AOD_{\lambda_L} = \int_{z_0}^z \alpha_t(\lambda_L, z)dz' \tag{A8}$$

Generally, we chose 7–9 km as the clear range, which means the aerosol hardly exists. On this assumption, the $\beta_t(z, \lambda_L) \approx \beta_m(z, \lambda_L)$. Additionally, the $AOD\lambda_L$ is used in AERONET data to replace the integral of the extinction coefficient Equation (A8). Finally, the lidar constant can be derived as Equation (A7).

Appendix A.3. Retrieval Method of Radar Backscatter

The radar equation is shown in Equation (A9), and the *RCS* can be expressed in Equation (A10).

$$P(z,\lambda_R) = \frac{C_R}{z^2}\beta_t(z,\lambda_R)\exp\left(-2\int_{z_0}^{z}\alpha_t(z,\lambda_R)dz'\right) \tag{A9}$$

$$RCS(z,\lambda_R) = C_R\beta_t(z,\lambda_R)\exp\left(-2\int_{z_0}^{z}\alpha_t(z,\lambda_R)dz'\right) \tag{A10}$$

where P_R is the received power detected at wavelength radar λ_R. C_R is the radar constant. β_t and α_t are the corresponding total backscatter coefficients and extinction coefficients at range z, respectively.

The β_t and α_t are presented in Equation (A11). The attunement for molecules is different than that detected by lidar, which is caused by the absorption of water droplets. The absorption of water is calculated by the ITU-R model. Therefore, the extinction-to-backscatter ratio for cloud particles (*RR*) is represented by Equation (A12):

$$\begin{aligned}\alpha_t &= \alpha_m + \alpha_p \\ \beta_t &= \beta_p\end{aligned} \tag{A11}$$

$$\alpha_p = RR \times \beta_p \tag{A12}$$

According to the Fernald forward method, the backscatter for the radar backscatter can be solved using Equation (A13):

$$\beta_R(\lambda_R,z) = \frac{RCS(\lambda_R,z)\exp\left(2\int_0^{\infty}\alpha_m(\lambda_R,z')dz'\right)}{C_R - 2\int_0^{z}RR(\lambda_R,z)RCS(\lambda_R,z)\exp\left(2\int_0^{\infty}\alpha_m(\lambda_R,z')dz'\right)dz} \tag{A13}$$

References

1. King, M.D.; Platnick, S.; Menzel, W.P.; Ackerman, S.A.; Hubanks, P.A. Spatial and Temporal Distribution of Clouds Observed by MODIS Onboard the Terra and Aqua Satellites. *IEEE Trans. Geosci. Remote Sens.* **2013**, *51*, 3826–3852. [CrossRef]
2. Morrison, H.; Lier-Walqui, M.; Fridlind, A.M.; Grabowski, W.W.; Harrington, J.Y.; Hoose, C.; Korolev, A.; Kumjian, M.R.; Milbrandt, J.A.; Pawlowska, H.; et al. Confronting the Challenge of Modeling Cloud and Precipitation Microphysics. *J. Adv. Model. Earth Syst.* **2020**, *12*, e2019MS001689. [CrossRef]
3. Liu, J.; Li, Z.; Zheng, Y.; Chiu, J.C.; Zhao, F.; Cadeddu, M.; Weng, F.; Cribb, M. Cloud Optical and Microphysical Properties Derived from Ground-Based and Satellite Sensors over a Site in the Yangtze Delta Region: Cloud Properties in Eastern China. *J. Geophys. Res. Atmos.* **2013**, *118*, 9141–9152. [CrossRef]
4. Tan, W.; Zhao, G.; Yu, Y.; Li, C.; Li, J.; Kang, L.; Zhu, T.; Zhao, C. Method to Retrieve Cloud Condensation Nuclei Number Concentrations Using Lidar Measurements. *Atmos. Meas. Tech.* **2019**, *12*, 3825–3839. [CrossRef]
5. Muskatel, H.B.; Blahak, U.; Khain, P.; Levi, Y.; Fu, Q. Parametrizations of Liquid and Ice Clouds' Optical Properties in Operational Numerical Weather Prediction Models. *Atmosphere* **2021**, *12*, 89. [CrossRef]
6. Krasnov, O.A.; Russchenberg, H.W.J. The relation between the radar to lidar ratio and the effective radius of droplets in water clouds: An analysis of statistical models and observed drop size distributions. In Proceedings of the 11th Conference on Cloud Physics 2002, Ogden, UT, USA, 2–7 June 2002; American Meteorological Society: Boston, MA, USA, 2002; pp. 1–9.
7. Shaw, M.A. Testing Lidar-Radar Derived Drop Sizes against In Situ Measurements. Master's Thesis, Michigan Technological University, Houghton, MI, USA, 2016.
8. Huang, D.; Zhao, C.; Dunn, M.; Dong, X.; Mace, G.G.; Jensen, M.P.; Xie, S.; Liu, Y. An Intercomparison of Radar-Based Liquid Cloud Microphysics Retrievals and Implications for Model Evaluation Studies. *Atmos. Meas. Tech.* **2012**, *5*, 1409–1424. [CrossRef]
9. Lamer, K.; Oue, M.; Battaglia, A.; Roy, R.J.; Cooper, K.B.; Dhillon, R.; Kollias, P. Multifrequency Radar Observations of Clouds and Precipitation Including the G-Band. *Atmos. Meas. Tech.* **2021**, *14*, 3615–3629. [CrossRef]
10. Vivekanandan, J.; Ghate, V.P.; Jensen, J.B.; Ellis, S.M.; Schwartz, M.C. A Technique for Estimating Liquid Droplet Diameter and Liquid Water Content in Stratocumulus Clouds Using Radar and Lidar Measurements. *J. Atmos. Ocean. Technol.* **2020**, *37*, 2145–2161. [CrossRef]
11. Hogan, R.J.; Illingworth, A.J.; O'Connor, E.J.; Bouniol, D.; Brooks, M.E.; Delanoë, J.; Donovan, D.P.; Eastment, J.D.; Gaussiat, N.; Goddard, J.W.F.; et al. Cloudnet: Evaluation of Model Clouds Using Ground-Based Observations. In Proceedings of the ECMWF Workshop on Parametrization of Clouds in Large-Scale Models, Reading, UK, 13–15 November 2006.

12. Radenz, M.; Bühl, J.; Lehmann, V.; Görsdorf, U.; Leinweber, R. Combining Cloud Radar and Radar Wind Profiler for a Value Added Estimate of Vertical Air Motion and Particle Terminal Velocity within Clouds. *Atmos. Meas. Tech.* **2018**, *11*, 5925–5940. [CrossRef]
13. Painemal, D.; Chiu, J.-Y.C.; Minnis, P.; Yost, C.; Zhou, X.; Cadeddu, M.; Eloranta, E.; Lewis, E.R.; Ferrare, R.; Kollias, P. Aerosol and Cloud Microphysics Covariability in the Northeast Pacific Boundary Layer Estimated with Ship-based and Satellite Remote Sensing Observations. *J. Geophys. Res. Atmos.* **2017**, *122*, 2403–2418. [CrossRef]
14. Lee, S.; Kahn, B.H.; Teixeira, J. Characterization of Cloud Liquid Water Content Distributions from CloudSat. *J. Geophys. Res.* **2010**, *115*, D20203. [CrossRef]
15. Khain, A.; Pinsky, M.; Magaritz, L.; Krasnov, O.; Russchenberg, H.W.J. Combined Observational and Model Investigations of the Z–LWC Relationship in Stratocumulus Clouds. *J. Appl. Meteorol. Climatol.* **2008**, *47*, 591–606. [CrossRef]
16. Oh, S.-B.; Lee, Y.H.; Jeong, J.-H.; Kim, Y.-H.; Joo, S. Estimation of the Liquid Water Content and Z-LWC Relationship Using Ka-Band Cloud Radar and a Microwave Radiometer: Estimation of the LWC Using Ka-Band Cloud Radar. *Met. Apps.* **2018**, *25*, 423–434. [CrossRef]
17. Baedi, R.J.P.; de Wit, J.J.M.; Russchenberg, H.W.J.; Erkelens, J.S.; Poiares Baptista, J.P.V. Estimating Effective Radius and Liquid Water Content from Radar and Lidar Based on the CLARE98 Data-Set. *Phys. Chem. Earth Part B Hydrol. Ocean. Atmos.* **2000**, *25*, 1057–1062. [CrossRef]
18. Fox, N.I.; Illingworth, A.J. The Retrieval of Stratocumulus Cloud Properties by Ground-Based Cloud Radar. *J. Appl. Meteorol.* **1997**, *36*, 8. [CrossRef]
19. Rémillard, J.; Kollias, P.; Szyrmer, W. Radar-Radiometer Retrievals of Cloud Number Concentration and Dispersion Parameter in Nondrizzling Marine Stratocumulus. *Atmos. Meas. Tech.* **2013**, *6*, 1817–1828. [CrossRef]
20. Hogan, R.J.; Brooks, M.E.; Illingworth, A.J.; Donovan, D.P.; Tinel, C.; Bouniol, D.; Baptista, J.P.V.P. Independent Evaluation of the Ability of Spaceborne Radar and Lidar to Retrieve the Microphysical and Radiative Properties of Ice Clouds. *J. Atmos. Ocean. Technol.* **2006**, *23*, 211–227. [CrossRef]
21. Tinel, C.; Testud, J.; Pelon, J.; Hogan, R.J.; Protat, A.; Delanoë, J.; Bouniol, D. The Retrieval of Ice-Cloud Properties from Cloud Radar and Lidar Synergy. *J. Appl. Meteorol.* **2005**, *44*, 860–875. [CrossRef]
22. Donovan, D.P.; Lammeren, A.C.A.P. van Cloud Effective Particle Size and Water Content Profile Retrievals Using Combined Lidar and Radar Observations: 1. Theory and Examples. *J. Geophys. Res. Atmos.* **2001**, *106*, 27425–27448. [CrossRef]
23. Okamoto, H. An Algorithm for Retrieval of Cloud Microphysics Using 95-GHz Cloud Radar and Lidar. *J. Geophys. Res.* **2003**, *108*, 4226. [CrossRef]
24. Weitkamp, C. (Ed.) *Lidar: Range-Resolved Optical Remote Sensing of the Atmosphere*; Springer Series in Optical Sciences; Springer: New York, NY, USA, 2005; ISBN 978-0-387-40075-4.
25. Rinehart, P.D.R.E. *Radar for Meteorologists*; Miss: Las Vegas, NV, USA, 2010; ISBN 978-0-9658002-3-5.
26. Mie, G. Beiträge zur Optik trüber Medien, speziell kolloidaler Metallösungen. *Ann. Phys.* **1908**, *330*, 377–445. [CrossRef]
27. Wu, W.; McFarquhar, G.M. Statistical Theory on the Functional Form of Cloud Particle Size Distributions. *J. Atmos. Sci.* **2018**, *75*, 2801–2814. [CrossRef]
28. Mao, F.; Gong, W.; Zhu, Z. Simple Multiscale Algorithm for Layer Detection with Lidar. *Appl. Opt.* **2011**, *50*, 6591. [CrossRef] [PubMed]
29. Shupe, M.D. A Ground-Based Multisensor Cloud Phase Classifier. *Geophys. Res. Lett.* **2007**, *34*, L22809. [CrossRef]
30. Porter, J.N.; Lienert, B.; Sharma, S.K. Using Horizontal and Slant Lidar Measurements to Obtain Calibrated Aerosol Scattering Coefficients from a Coastal Lidar in Hawaii. *J. Atmos. Ocean. Technol.* **2000**, *17*, 10. [CrossRef]
31. Gunn, K.L.S.; East, T.W.R. The Microwave Properties of Precipitation Particles. *Q. J. R. Met. Soc.* **1954**, *80*, 522–545. [CrossRef]
32. Kedenburg, S.; Vieweg, M.; Gissibl, T.; Giessen, H. Linear Refractive Index and Absorption Measurements of Nonlinear Optical Liquids in the Visible and Near-Infrared Spectral Region. *Opt. Mater. Express* **2012**, *2*, 1588. [CrossRef]
33. Misumi, R.; Uji, Y.; Tobo, Y.; Miura, K.; Uetake, J.; Iwamoto, Y.; Maesaka, T.; Iwanami, K. Characteristics of Droplet Size Distributions in Low-Level Stratiform Clouds Observed from Tokyo Skytree. *J. Meteorol. Soc. Jpn.* **2018**, *96*, 405–413. [CrossRef]
34. Miles, N.L.; Verlinde, J.; Clothiaux, E.E. Cloud Droplet Size Distributions in Low-Level Stratiform Clouds. *J. Atmos. Sci.* **2000**, *57*, 17. [CrossRef]
35. Deng, Z.; Zhao, C.; Zhang, Q.; Huang, M.; Ma, X. Statistical Analysis of Microphysical Properties and the Parameterization of Effective Radius of Warm Clouds in Beijing Area. *Atmos. Res.* **2009**, *93*, 888–896. [CrossRef]
36. Moriasi, D.N.; Arnold, J.G.; Van Liew, M.W.; Bingner, R.L.; Harmel, R.D.; Veith, T.L. Model Evaluation Guidelines for Systematic Quantification of Accuracy in Watershed Simulations. *Trans. ASABE* **2007**, *50*, 885–900. [CrossRef]
37. Atlas, D. The estimation of cloud parameters by radar. *J. Atmos. Sci.* **1954**, *11*, 309–317. [CrossRef]
38. Che, Y.; Ma, S.; Xing, F.; Li, S.; Dai, Y. An Improvement of the Retrieval of Temperature and Relative Humidity Profiles from a Combination of Active and Passive Remote Sensing. *Meteorol. Atmos. Phys.* **2019**, *131*, 681–695. [CrossRef]